Using Physics-Based Macroscopic and Microscopic Mixture Models for Hyperspectral Pixel Unmixing

Ryan Close[a], Paul Gader[a], Joseph Wilson[a], Alina Zare[b]

[a]Department of Computer and Information Science and Engineering, University of Florida, Gainesville, FL, USA;

[b]Department of Electrical and Computer Engineering, University of Missouri, Columbia, MO, USA

ABSTRACT

A method of incorporating macroscopic and microscopic reflectance models into hyperspectral pixel unmixing is presented and discussed. A vast majority of hyperspectral unmixing methods rely on the linear mixture model to describe pixel spectra resulting from mixtures of endmembers. Methods exist to unmix hyperspectral pixels using nonlinear models, but rely on severely limiting assumptions or estimations of the nonlinearity. This paper will present a hyperspectral pixel unmixing method that utilizes the bidirectional reflectance distribution function to model microscopic mixtures. Using this model, along with the linear mixture model to incorporate macroscopic mixtures, this method is able to accurately unmix hyperspectral images composed of both macroscopic and microscopic mixtures. The mixtures are estimated directly from the hyperspectral data without the need for *a priori* knowledge of the mixture types. Results are presented using synthetic datasets, of macroscopic and microscopic mixtures, to demonstrate the increased accuracy in unmixing using this new physics-based method over linear methods. In addition, results are presented using a well-known laboratory dataset. Using these results, and other published results from this dataset, increased accuracy in unmixing over other nonlinear methods is shown.

Keywords: Hyperspectral image analysis, physics-based mixture models, reflectance spectroscopy, nonlinear unmixing, microscopic mixture, macroscopic mixture, multi-mixture pixel

1. INTRODUCTION

A common research problem in hyperspectral image (HSI) analysis is that of estimating endmember proportions from a given set of pixels, often referred to as pixel unmixing.[1-17] A vast majority of approaches to this problem rely on a linear model to describe the mixing relationships between endmembers.[1] An example is the linear mixture model (LMM) shown in Equation (1), with the corresponding constraints in Equation (2), where M is the number of endmembers in the scene, ϵ_i is an error term, and e_k and p_{ik} are the endmembers and proportions, respectively, of a given pixel x_i.[2, 3] Reliance on the linear model is a result of the mathematical amenability of linear models and the prevalence of macroscopic mixtures, also known as areal or checkerboard mixtures. Macroscopic mixtures occur when two or more endmembers are discretely present within the instantaneous field of view of a given pixel.[1] This mixing is caused by the coarse spatial resolution of the hyperspectral sensor and does not represent a physical mixing of endmembers.

$$x_i = \sum_{k=1}^{M} e_k p_{ik} + \epsilon_i \tag{1}$$

$$\forall_{ik}\ p_{ik} \geq 0 \quad \forall_i \sum_{k=1}^{M} p_{ik} = 1 \tag{2}$$

Research, however, has shown that nonlinear mixtures are present in hyperspectral images and have a substantial effect on measured spectral reflectance signatures over a given image.[1, 18, 19] Recently the impact of nonlinear mixtures in HSIs has garnered much attention.[1, 18-52] Keshava and Mustard describe the effects of nonlinear mixing by stating[1]:

> In tests of linear versus nonlinear mixing on laboratory data, the fractions calculated may be in error by as much as 30% absolute. In addition, the linear model can cause considerable ambiguity and false fractions when used on nonlinear mixtures. Absorption bands and continua in nonlinear mixtures cannot be adequately fit with a linear model.

Microscopic mixtures, also called intimate mixtures, are known to be present in many hyperspectral images. [1, 40, 53-62] Unlike the macroscopic mixture, microscopic mixtures form non-linear mixtures of endmember spectra. [54-57, 61, 62] Consequently, the LMM has been shown inadequate for modeling this type of mixing in hyperspectral data. [1, 40, 53-62] While microscopic mixing does represent physical mixtures of endmembers, it is important to note that it is not a chemical reaction (i.e., the constituent endmember substances still exist).

Attempts to incorporate the nonlinearity of microscopic mixtures into the hyperspectral pixel unmixing problem have been largely black-box approaches. Traditional methods of reproducing an unknown nonlinear function such as neural networks [33, 37-39] and kernel methods [41, 49, 59, 60, 63-65] have been used to estimate the latent nonlinear function in the system. Recent research has introduced manifolds to model the nonlinearity in hyperspectral data.[20, 22-28, 46-48, 51, 52, 66-81] Typically used in hyperspectral classification applications, endmember and proportion estimation has also been pursued with manifold based algorithms. [35, 36, 82] These methods all attempt to account for the nonlinearity with a generic machine learning model to approximate the mixture; however they do not explicitly model the underlying physics of the mixture.

Two commonly referenced physics-based techniques for microscopic mixture pixel unmixing are Mustard and Pieters's least squared error (LSE) unmixing of single-scattering albedo data[53] and Guilfoyle, et al. use of a radial basis function neural network (RBFNN)[33]. However, these methods of microscopic mixture pixel unmixing require the assumption that a data set contains only macroscopically mixed data or microscopically mixed data. [33, 40, 53, 54, 83-85]

Recently, two methods for pixel unmixing were developed that allow for proportion estimation in the presence of both macroscopic and microscopic mixtures. The first is a physics-based kernel approach that approximates Hapke's reflectance model. [59, 60, 63] The second is the microscopic mixture iterated constrained endmembers (MICE) algorithm.[86] These two approaches, however, assume that a given HSI pixel is composed exclusively of a single mixture type (i.e. either macroscopically or microscopically mixed). This assumption is valid for some HSIs. However, the assumption is violated in HSIs that contain overlapping heterogeneous regions of different mixture types. In these scenes a pixel may be composed of a macroscopic mixture, a microscopic mixture, or a combination of the two mixture types. A second violation to this assumption occurs when one or more endmembers of a microscopic mixture clump together. These particles cause macroscopic mixing with the surrounding microscopic mixture. These observations led to a new HSI pixel model, the multi-mixture pixel (MMP). The MMP characterizes a pixel as a macroscopic mixture of endmembers and a microscopic mixture, i.e., a mixture of mixtures.

The remainder of this paper is organized as follows. Section II gives a review of microscopic mixtures and the bidirectional reflectance distribution function (BRDF). Next, in Section III the MMP model is discussed and the associated MMP proportion estimation (MPE) algorithm is introduced. Section IV presents experimental results on both synthetic data sets and well-known sets of laboratory mineral mixtures, the RELAB data sets. Using the RELAB data, MPE is compared to the previously mentioned LSE, RBFNN, MICE, and physics-based kernel approaches to unmixing microscopically mixed data. Additionally, MPE is contrasted to proportions estimated using the LMM and a popular neural network approach for unmixing nonlinear hyperspectral mixed pixels, the Hopfield neural network/ multi-layer perceptron (HNN/MLP) of Plaza, et al.[38] Finally, in Section V conclusions and future research is discussed.

2. REVIEW OF MICROSCOPIC MIXTURES

Microscopic mixing occurs when particles of different endmembers are homogenously distributed within the instantaneous field of view of a given pixel. Light incident on this mixed surface is scattered.[56, 61] The close proximity of endmembers particles, occurring in a microscopic mixture, causes multi-scattering between particles with differing spectral properties. [1, 54] This multi-scattering between particles causes a nonlinear mixture in reflectance spectra. To accurately estimate endmembers and proportions within the context of microscopic mixture reflectance spectra, a model for reflectance is needed.

Reflectance is characterized by the collimation of the light source and the detector (or sensor). Because perfect collimation and perfect diffuseness do not exist, in reality all reflectances are biconical. [56, 61] However, on a clear, sunny day, the sun can be reasonably approximated as a collimated source (i.e., directional). [56] An air or space borne sensor looking at the ground approximates a directional detector. [56] Therefore, under these basic remote sensing assumptions (including assuming minimal cloud cover), the BRDF is the appropriate model for hyperspectral image applications.

Hapke's BRDF has been validated through experimentation and is widely accepted as an accurate model. [33, 38, 40, 41, 53-63, 83-85] Hapke's reflectance coefficient BRDF is given by Equation (3), where c_i and c_e are the cosine of the angles of incidence and emergence, respectively, g is the phase angle, $P(g)$ is the phase function for particles, $B(g)$ is the

backscatter function given by Equation (4), $H(\mu)$ is Hapke's approximation to Chandrasekhar's function for isotropic multi-scattering given by Equation (5), and w is the average single-scattering albedo given by Equation (6) with P_S and P_A being the power of the incident irradiance scattered and absorbed by the particle, respectively. [33, 53-56, 59-61, 63] To clarify terms, c_i and c_e are used for the cosine of the angles of incidence and emergence instead of the traditional μ_0 and μ. The phase angle and the angles of incidence and emergence describe the geometries of the light source and detector. Scattering properties of the surface are described by the $P(g)$ function. The backscatter function $B(g)$ models the opposition effect, as given by Equation (4) where B_0 describes the magnitude of the opposition effect and h depends on the interparticle spacing.

$$R = \frac{w}{4(c_i + c_e)}\{[1 + B(g)]P(g) + H(c_i)H(c_e) - 1\} \tag{3}$$

$$B(g) = \frac{B_0}{1 + \left(\frac{1}{h}\right)tan\left(\frac{g}{2}\right)} \tag{4}$$

$$H(c_{[i,e]}) = \frac{1 + 2c_{[i,e]}}{\left(1 + 2c_{[i,e]}(1 - w_\lambda)^{1/2}\right)} \tag{5}$$

$$w = \frac{P_S}{P_S + P_A} \tag{6}$$

Under remote sensing assumptions, the angle of incidence is commonly 15^0 to 40^0 and the angle of emergence 0^0, under these conditions the phase angle is between 15^0 and 40^0. [53] Additionally, under remote sensing assumptions, these angles are assumed constant over a given collection. Mustard and Pieters demonstrated that at phase angles greater than 15^0 the $B(g)$ was negligible. [53] Additionally, under the assumption of isotropic scattering (all light is scattered equally in all directions) the phase function is defined to be $P(g) = 1$. [56, 61] Using these remote sensing assumptions and the consequential results for $B(g)$ and $P(g)$, a simplified reflectance coefficient function can be derived as shown in Equation (7) where the λ subscript is used to signify the wavelength dependence of the reflectance function. Also, w_λ was added as a parameter to Chandrasekhar's function to represent the single-scattering albedo as an input parameter to the function. As the reflectance coefficient function, under the described assumptions, is the only model for reflectance used in this research it will simply be referred to as the reflectance function. The resulting reflectance function can be seen plotted against single-scattering albedo in Figure 1.

$$R_\lambda = \frac{w_\lambda}{4(c_i + c_e)}H(c_i, w_\lambda)H(c_e, w_\lambda) \tag{7}$$

The reflectance of a microscopic mixture is described by the reflectance function (Equation (7)) and the average single-scattering albedo of the mixture, shown in Equation (8). [53, 54, 56] The average single-scattering albedo is a linear combination of endmember's single-scattering albedos where Ψ_k, q_k, and d_k are the mass fraction, single particle density, and average effective particle size for a given mixture component (i.e., endmember). [56]

$$w_\lambda = \frac{\sum_{k=1}^{M}(\Psi_k/q_k d_k)\, w_{k\lambda}}{\sum_{k=1}^{M}(\Psi_k/q_k d_k)} \tag{8}$$

The average single-scattering albedo can also be represented as a relative geometric cross-section (F_k) or endmember proportion (f_k), shown in Equation (9) for the kth component. [56] This representation is important, because often in remote sensing the particle density and particle size of endmembers is not known. Therefore, the particle density and particle size are assumed roughly equal for all endmembers. Under this assumption, the proportion of an endmember composing a mixed pixel's spectra (i.e., the relative geometric cross-section of the pixel composed of the endmember) is equal to its mass fraction.

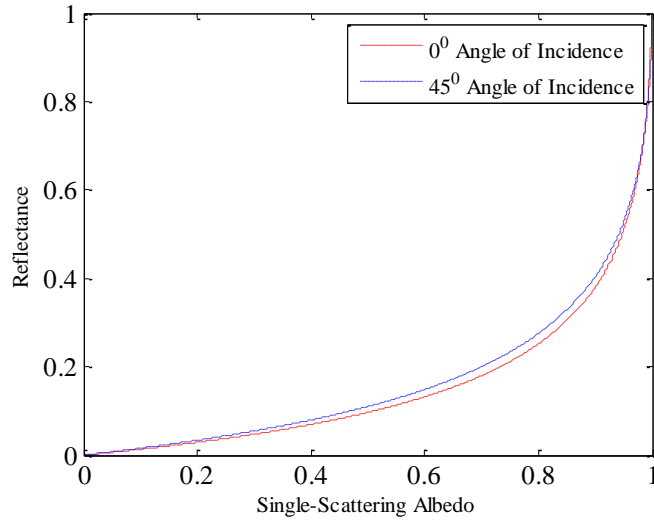$$F_k = f_k = \frac{(\Psi_k/q_k d_k)}{\sum_{k=1}^{M}(\Psi_k/q_k d_k)} \tag{9}$$

Figure 1: Reflectance function curve versus single-scattering albedo (angle of emergence is 0^0).

Using the relative geometric cross-section representation for each endmember, the equation for the average single-scattering albedo can be written as Equation (10). This formulation leads to constraints similar to those of the LMM: $f_k \geq 0$ and $\sum_{k=1}^{M} f_k = 1$. Additionally, the albedo-domain formulation given in Equation (10) can be represented in the reflectance-domain as shown by Equation (11), with the same constraints.

$$w_\lambda = \sum_{k=1}^{M} f_k w_{k\lambda} \tag{10}$$

$$x_i = R\left(\sum_{k=1}^{M} f_{ik} w_k\right) \tag{11}$$

3. MULTI-MIXTURE PIXELS

3.1 Multi-Mixture Pixel Model

The MMP model, shown in Equation (12), characterizes a pixel as a macroscopic mixture of endmembers and a microscopic mixture, i.e., a mixture of mixtures. The MMP model (Equation (12)) has not been previously considered in HSI analysis.

$$x_i = \sum_{k=1}^{M} p_{ik} e_k + p_{iM+1} R\left(\sum_{k=1}^{M} f_{ik} w_k\right) + \varepsilon_i \tag{12}$$

The macroscopic proportions (p_{ik}) in the MMP model are dependent on the reflectance of the component microscopic mixture. Therefore, the macroscopic proportions are dependent on the microscopic proportions (f_{ik}). Estimation of the microscopic proportions is an ill-posed inversion problem. Ignoring noise, consider the following case, as illustrated in Figure 2. An MMP x is composed of two endmembers, e_1 and e_2. The MMP mixture point is constrained by the set of possible macroscopic mixtures between the endmembers, illustrated as a dashed blue line, and the set of possible microscopic mixtures between the endmembers, illustrated as a solid red curve. Recall that the MMP model treats the microscopic mixture as an endmember. Therefore, the MMP model can represent x with 0 residual error using e_1, e_2, and $r = R(\sum_{k=1}^{M} f_{ik} w_k)$ for any point r on the arc A. More precisely, $\forall r \in A \, \exists \, p_{1,}, p_2, p_3 : x = p_1 e_1 + p_2 e_2 + p_3 r$.

As a pixel's microscopic mixture proportion (p_{iM+1}) increases, the MMP mixture point moves closer to the microscopic mixture line, as shown in Figure 3. Therefore, the plausible proportions of the microscopic mixture become increasingly constrained and even unique in the case of a 100% microscopic mixture, i.e., the arc A of plausible points r shrinks. As an MMP mixture point's microscopic mixture proportion lessens, the MMP mixture point moves closer to the macroscopic mixture, as shown in Figure 4. This causes the plausible microscopic proportions to be less constrained,

i.e., the arc $\boldsymbol{A}$ of plausible points $\boldsymbol{r}$ increases. However, as the microscopic mixture proportion decreases (i.e., the MMP is dominated by a macroscopic mixture) the microscopic mixture becomes less of a factor in the overall pixel's mixture proportions. Therefore, the error caused by the ill-posed inversion of estimating the microscopic proportions is a small factor in accurately estimating the mixture proportions.

3.2 MMP Proportion Estimation

Estimating proportions of the MMP model, termed MMP proportion estimation (MPE), is composed of two steps. First, the reflectance signature of the microscopic mixture component of the MMP must be estimated. To determine this reflectance signature, the microscopic mixture proportions are estimated using an albedo-domain microscopic mixture, given by Equation (13). This albedo-domain microscopic mixture term is derived from Equation (11), where $\boldsymbol{\beta}_i$ is an assumed zero-mean Gaussian additive noise term. .[1, 2, 53, 54, 59, 60, 63, 87] Estimation of the microscopic mixture proportions is accomplished by using quadratic programing to minimize the residual sum of squares (RSS) of Equation (13), as shown in Equation (14), with its associated constraints. Secondly, the macroscopic proportions are estimated by minimizing the RSS objective function shown in Equation (15), derived from the MMP model (Equation (12)). When estimating the macroscopic mixture proportions, the microscopic mixture proportions are held fixed.

$$\mathrm{R}^{-1}(\boldsymbol{x}_i) = \sum_{k=1}^{M} f_{ik} \boldsymbol{w}_k + \boldsymbol{\beta}_i \tag{13}$$

$$\mathbf{RSS} = \sum_{i=1}^{N} \left(\left(\mathbf{R}^{-1}(\boldsymbol{x}_i) - \sum_{k=1}^{M} \boldsymbol{f}_{ik}\boldsymbol{w}_k \right)^T \left(\mathbf{R}^{-1}(\boldsymbol{x}_i) - \sum_{k=1}^{M} \boldsymbol{f}_{ik}\boldsymbol{w}_k \right) \right) \tag{14}$$

$$\mathbf{RSS} = \sum_{i=1}^{N} \left(\left(\boldsymbol{x}_i - \sum_{k=1}^{M} p_{ik}\boldsymbol{e}_k - p_{iM+1}\mathbf{R}\left(\sum_{k=1}^{M} \boldsymbol{f}_{ik}\boldsymbol{w}_k \right) \right)^T \left(\boldsymbol{x}_i - \sum_{k=1}^{M} p_{ik}\boldsymbol{e}_k - p_{iM+1}\mathbf{R}\left(\sum_{k=1}^{M} \boldsymbol{f}_{ik}\boldsymbol{w}_k \right) \right) \right) \tag{15}$$

The final MPE algorithm is as follows:

1. Take as input a set of pixels from an HSI and a set of endmembers

2. Use quadratic programming to estimate the microscopic mixture proportions (f_{ik}'s) by minimizing the RSS in Equation (14)

3. Use quadratic programming to estimate the macroscopic mixture proportions (p_{ik}'s) by minimizing the RSS in Equation (15)

The resulting proportions are interpreted as follows. The macroscopic proportions *1* through *M* ($p_{i1} \cdots p_{iM}$) represent the proportions of endmembers macroscopically mixed. The *M+1* macroscopic proportion (p_{iM+1}) is the estimated proportion of the pixel composed of a microscopic mixture. Therefore, $p_{iM+1}f_{ik}$ is the proportion of the pixel described by a microscopic mixture of the kth endmember.

Returning to the diagram in Figure 2, the estimated microscopic mixture proportions result in a point $\boldsymbol{r}$ on the arc $\boldsymbol{A}$ that is the closest to the MMP mixture point. The estimated macroscopic mixture proportions find a minimal RSS solution within the simplex formed by the endmembers and the previously estimated point $\boldsymbol{r}$. Typically, a unique estimation of the microscopic mixture proportions is not possible with the information contained within a given HSI pixel. Therefore, it is probable that some amount of estimation error will be introduced into the microscopic proportion estimation. This introduced error is due to the ill-posed inversion and is unavoidable in estimating proportions in the MMP model using only HSI spectral information.
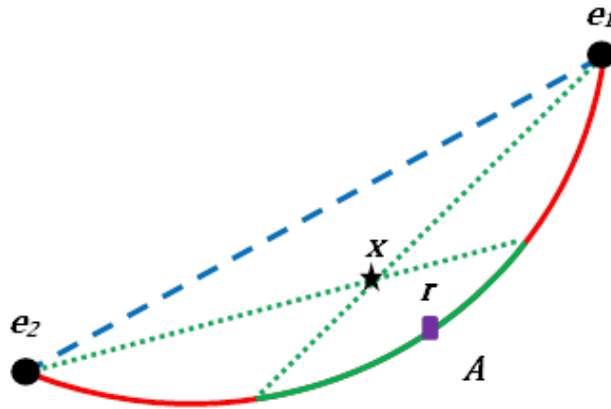
Figure 2: Diagram of multi-mixture pixel (black star) contained within the region bounded by the possible macroscopic mixtures (dashed blue line) and the possible microscopic mixtures (solid red curve) with plausible constituent microscopic mixture point (purple square).
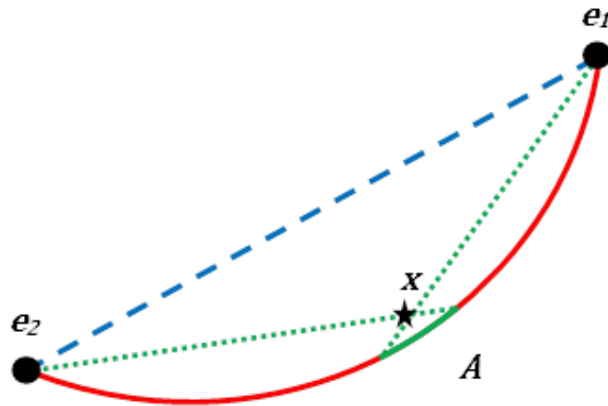

Figure 3: Diagram of multi-mixture pixel x contained within the region bounded by the possible macroscopic mixtures (dashed blue line) and the possible microscopic mixtures (solid red curve) with plausible constituent microscopic mixtures (green arc).

Figure 4: Diagram of multi-mixture pixel x contained within the region bounded by the possible macroscopic mixtures (dashed blue line) and the possible microscopic mixtures (solid red curve) with plausible constituent microscopic mixtures (green arc).
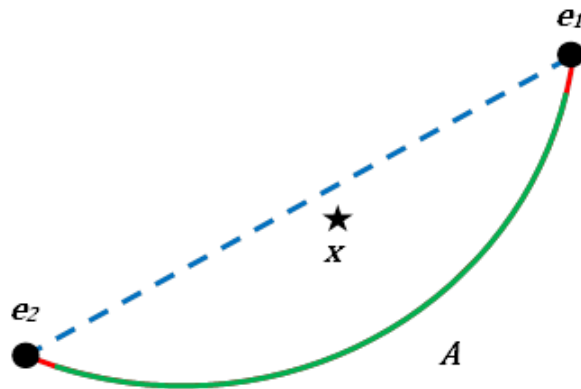
4. EXPERIMENTAL RESULTS

A quantitative investigation of the proposed algorithm was conducted using sets of synthetically created data sets and the RELAB data sets of known mineral mixtures. The MPE algorithm was compared to results obtained by estimating proportions using the LMM and an albedo-domain LMM (AD-LMM) algorithm. LMM proportions were estimated using quadratic programming to minimize the RSS term given in Equation (16), derived from the LMM shown in

Equation (1). Similarly, the AD-LMM proportions were estimated using quadratic programming to minimize the RSS term given in Equation (14), derived from Equation (13). Thus, allowing a comparison between MPE and proportions estimated with the LMM in both reflectance and albedo-domains. For convenience, the proportion estimation algorithms using quadratic programming to minimize the RSS terms derived from the LMM and AD-LMM models will simply be referred to by their underlying models, i.e. LMM and AD-LMM.

$$RSS = \sum_{i=1}^{N} \left(\left(x_i - \sum_{k=1}^{M} p_{ik} e_k \right)^T \left(x_i - \sum_{k=1}^{M} p_{ik} e_k \right) \right) \tag{16}$$

To evaluate error in estimating proportions, the root mean square error (RMSE) shown in Equation (17) was used, where N is the number of data set samples, M is the number of endmembers, a_{ik} is the true proportion of the sample, and $\hat{a}_{ik}$ is the estimated proportion. [33, 38, 53, 59, 60] The sample proportion estimates are calculated for data sets containing macroscopic, microscopic, and MMP mixtures as given by Equation (18), where $\hat{p}_{ik}$ and $\hat{f}_{ik}$ are the estimated macroscopic and microscopic mixture proportions, respectively. Each algorithm being evaluated took as input the correct endmember spectra for each data set. [33, 38, 53, 59, 60]

$$RMSE = \left(\frac{1}{N \cdot M} \sum_{i=1}^{N} \sum_{k=1}^{M} (a_{ik} - \hat{a}_{ik})^2 \right)^{\frac{1}{2}} \tag{17}$$

$$\hat{a}_{ik} = \hat{p}_{ik} + \hat{p}_{iM+1} \hat{f}_{ik} \tag{18}$$

4.1 Synthetic Data Sets Results

Each synthetic data set is composed of 1,000 data points created using three 38-dimensional endmembers obtained from the ASTER spectral library.[88] Four categories of synthetic data sets where used: macroscopic only, microscopic only, combined macroscopic and microscopic (CMM), and MMP. The CMM data sets were formed from the union of 500 independently created mixture data points from each of the macroscopic and microscopic mixtures. The MMP data set was created using the MMP model, Equation (12). The macroscopic and microscopic proportions for each category of synthetic data sets were drawn from a uniform distribution. Independent zero-mean Gaussian noise, with standard deviation of .001, was added to each mixture data point.

In these experiments 50 data sets were generated from each synthetic data set category. The standard deviation of proportion estimates was less than .01 in all cases. This, of course, is expected due to the fact that as long as the endmembers are linearly independent, quadratic programming produces a unique global minimizer. In evaluating proportion estimation accuracy the true endmembers were used.

In evaluating the proportion estimation accuracy of MPE, two important results must be assessed. The first is the accuracy in which MPE estimated the amount of microscopic mixing present in the data set.

Table 1 shows the mean percentage that MPE, MICE, LMM, and AD-LMM estimated each data set category as microscopically mixed. Neither LMM nor AD-LMM has an ability to label a pixel as macroscopically or microscopically mixed. Therefore, their results are 0% and 100%, respectively. As MICE is only able to label a pixel as either macroscopically or microscopically mixed, the reported mean estimated percentage microscopic mixture is the mean percentage of pixels labeled as a microscopic mixture. Secondly, the RMSE of the endmembers estimated proportions must be evaluated. Table 2 gives the mean proportion estimation RMSE for each algorithm over all four data set categories.

	Macroscopic Mixture	CMM	Microscopic Mixture	MMP
Truth	0.0%	50.0%	100.0%	25.0%
MPE	0.7%	49.6%	98.4%	18.9%
MICE	0.0%	49.9%	99.9%	4.1%
LMM	0.0%	0.0%	0.0%	0.0%
AD-LMM	100.0%	100.0%	100.0%	100.0%

Table 1: Mean estimated percentage microscopic mixture of synthetic data sets using MPE, MICE, LMM, and AD-LMM.

	Macroscopic Mixture	CMM	Microscopic Mixture	MMP
MPE	0.2%	0.2%	0.2%	1.2%
MICE	0.1%	0.1%	0.2%	3.2%
LMM	0.1%	6.7%	13.3%	3.5%
AD-LMM	15.9%	8.0%	0.2%	13.6%

Table 2: Mean estimated proportions RMSE of synthetic data sets using MPE, MICE, LMM, and AD-LMM.

From both the percentage microscopic mixture and proportion estimation results, it can be observed that when a data set is composed of only macroscopic mixtures, MPE, MICE and LMM perform similarly. Likewise, when the data set is composed of only microscopic mixtures, MPE, MICE, and AD-LMM perform similarly. However, when the dataset is composed of both mixture types (i.e., the CMM data set), neither LMM nor AD-LMM is able to estimate the proportions accurately. In contrast both MPE and MICE still produce an accurate estimation of proportions. Likewise, LMM and AD-LMM produced large errors when run on microscopic mixture data and macroscopic mixture data, respectively. Evaluation of the results indicates neither MICE, LMM, nor AD-LMM were able to accurately estimate the proportions of the MMP data sets. MPE, however, demonstrated increased accuracy in estimating both the percentage of a data set microscopically mixed as well as the mixture proportions.

4.2 RELAB Data Sets Results

The RELAB data sets used consist of mixtures of Enstatite with Olivine and Magnetite with Olivine. These mixtures where prepared and measured by Professors John Mustard and Carle Pieters of Brown University, as specified in their paper.[53] The spectra were collected with RELAB, a high-resolution bidirectional reflectance spectrometer with a specified angle of emergence of 0^0 and angle of incidence of 30^0.[53] Each mixture data set is composed of spectra from five mixed samples and two endmembers. The spectra have 211 dimensions with wavelengths ranging from 400 nm to 2,500 nm. These data sets have become a *de facto* standard for evaluating microscopic unmixing algorithms.[33, 38, 53, 59, 60]

The RELAB proportion estimation results are shown in Table 3, part A shows results from the Enstatite & Olivine mixture and part B the Magnetite & Olivine mixture. Proportion RMSE results were included from or calculated from published results using the (*)LSE[53], (**)kernel methods[59, 60, 63], (***)RBFNN[33], and (****)HNN/MLP[38] algorithms.

Method	(A) Enstatite & Olivine		(B) Magnetite & Olivine	
	F-Parameter Proportion RMSE	Mass Fraction Proportion RMSE	F-Parameter Proportion RMSE	Mass Fraction Proportion RMSE
MPE	0.0118	0.0120	0.0219	0.0229
MICE	0.0136	0.0131	0.0135	0.0123
LMM	0.0389	0.0399	0.2790	0.2873
*LSE	0.0267	0.0265	0.0193	0.0202
**RBF Kernel		0.0345		0.2101
**Polynomial Kernel		0.0158		0.1658
**Physics-based Kernel		0.0228		0.0561
**Areal/Intimate Kernel		0.0197		0.0589
***RBFNN	0.0306	0.0337	0.0318	0.0490
****HNN/MLP	0.0171	0.0168	0.0802	0.0754

Table 3: Estimated proportion RMSE for RELAB mineral data sets.

In the published works using kernel methods and neural networks to unmix microscopically mixed hyperspectral data, RMSE comparisons were made using the known mass fractions of the RELAB samples.[33, 38, 59, 60] However, since these unmixing algorithms estimate microscopic mixture proportions, often referred to as F-parameters, an assumption of similar particle densities and diameters between endmembers is required.[53, 56, 61] This relationship can be observed in Equation (9). The RELAB data sets were prepared such that particle diameters are similar but not particle densities.[53] Therefore, a more appropriate measure of accuracy in estimating RELAB proportions is to calculate RMSE between estimated proportions and published F-parameters for the data sets.

Table 3 lists proportion RMSEs between published LSE, RBFNN, and HNN/MLP estimated proportions and F-parameter truth for comparison with the experimentally estimated MPE, MICE, and LMM proportions.[33, 38, 53] However, the estimated proportions using the various kernel methods were not available.[59, 60] Therefore, the proportion RMSE using mass fractions is given, as published, for the kernel and neural network approaches.[33, 38, 59, 60] Using the

known F-parameters and mass fractions, as recorded by Mustard and Pieters [53] , the particle densities of each mineral can be estimated. The particle densities are used with the MPE, MICE, and LMM estimated F-parameters of each data set to estimate the correct mass fraction estimate for each sample. Using these mass fraction estimates the MPE, MICE, and LMM mass fraction RMSE can be compared with the reported mass fraction RMSE of the previously mentioned papers.

In evaluating the results of the Enstatite with Olivine RELAB data set, MPE estimated the mixture proportions with the least amount of error; outperforming even the MICE and LSE algorithms. This result is significant in that even though these two minerals are known to mix microscopically. It has been observed that they partially mix linearly in this data set.[59] The results of the Magnetite with Olivine RELAB data set reveal that the MICE and LSE algorithms produce more accurate estimations of the mixture proportions than does MPE, although MPE outperforms the remaining algorithms. This result can be understood from the known error introduced by MPE during the ill-posed inversion problem of estimating the microscopic mixture proportions. As this RELAB data set is strongly microscopically mixed, the MICE and LSE algorithms are perfectly suited to estimate the proportions of this strictly microscopic mixture data set.

5. CONCLUSIONS AND FUTURE WORK

In this paper a new model was presented to describe an HSI pixel that may be composed of more than one mixture type, the MMP model. An associated algorithm, MPE, was presented to estimate proportions of HSI pixels using the MMP model. Using synthetic data sets, it was demonstrated that pixels composed of multiple mixture types create increased error in estimating mixture proportions when using a linear model, or even the MICE algorithm. Through experimentation it was shown that MPE is able to accurately estimate the mixture proportions of data sets composed of macroscopic mixtures, microscopic mixtures, combined macroscopic and microscopic mixtures, and multiple mixtures. Further analysis was done using the RELAB laboratory data sets of known microscopic mixtures. Using these data sets MPE was compared against existing methods for unmixing microscopic mixtures. Analysis revealed that MPE was able to accurately unmix the RELAB data sets. As would be expected, it outperformed all algorithms on data that contained partially linear and nonlinear (microscopic) mixtures. However, showed increased error compared to MICE and LSE on data sets that were strictly microscopically mixed. In conclusion, MPE was shown to be a robust algorithm for unmixing HSI data of multiple mixture types or unknown mixtures types.

Ongoing research is focused on alternating methods of optimizing the MPE objective function to allow for simultaneous estimation of endmembers. Future work could incorporate HSI spatial information to the microscopic proportion estimation thereby smoothing the proportion map of the microscopic mixing proportion. This would bring more information to the ill-posed inversion problem and potentially reduce the introduced error. Also, future research could utilize LiDAR sensor data to increase the accuracy in estimating the angles of incidence and emergence used in the BRDF.

REFERENCES

[1]   Keshava, N. and Mustard, J. F., "Spectral unmixing", Signal Processing Magazine, IEEE, 19(1), 44-57 (2002).
[2]   Berman, M., Kiiveri, H., et al., "ICE: a statistical approach to identifying endmembers in hyperspectral images", Geoscience and Remote Sensing, IEEE Transactions on, 42(10), 2085-2095 (2004).
[3]   Zare, A. and Gader, P., "Sparsity Promoting Iterated Constrained Endmember Detection in Hyperspectral Imagery", Geoscience and Remote Sensing Letters, IEEE, 4(3), 446-450 (2007).
[4]   Bioucas-Dias, J. M., "A variable splitting augmented Lagrangian approach to linear spectral unmixing", Hyperspectral Image and Signal Processing: Evolution in Remote Sensing, 2009. WHISPERS '09. First Workshop on, 1-4 (2009)
[5]   Boardman, J. W., "Automating spectral unmixing of AVIRIS data using convex geometry concepts", Summaries of the Fourth Annual JPL Airborne Geoscience Workshop, JPL Pub. 93-26, AVIRIS Workshop, 1(11-14 (1993).
[6]   Boardman, J. W., Kruse, F. A., et al., "Mapping Target Signatures Via Partial Unmixing of AVIRIS Data", Summaries, Fifth JPL Airborne Earth Science Workshop, JPL Publications, 1(23-26 (1995).
[7]   Nascimento, J. M. P. and Dias, J. M. B., "Vertex component analysis: a fast algorithm to unmix hyperspectral data", Geoscience and Remote Sensing, IEEE Transactions on, 43(4), 898-910 (2005).

[8]   Santos-Garcia, A. and Velez-Reyes, M., "Identifiability of geometric models for linear unmixing at different spatial resolutions in hyperspectral unmixing", Hyperspectral Image and Signal Processing: Evolution in Remote Sensing (WHISPERS), 2010 2nd Workshop on, 1-4 (2010)

[9]   Tsung-Han, C., Wing-Kin, M., et al., "Hyperspectral unmixing from a convex analysis and optimization perspective", Hyperspectral Image and Signal Processing: Evolution in Remote Sensing, 2009. WHISPERS '09. First Workshop on, 1-4 (2009)

[10]   Winter, M. E., "N-FINDR: An Algorithm for Fast Autonomous Spectral End-member Determination in Hyperspectral Data", SPIE Conference on Imaging Spectrometry V, 266-275 (1999)

[11]   Xiaoli, J., Yingzi, D., et al., "Component analysis-based unsupervised linear spectral mixture analysis for hyperspectral imagery", Hyperspectral Image and Signal Processing: Evolution in Remote Sensing, 2009. WHISPERS '09. First Workshop on, 1-5 (2009)

[12]   Dobigeon, N., Moussaoui, S., et al., "Bayesian separation of spectral sources under non-negativity and full additivity constraints", Signal Processing, 89(12), 2657-2669 (2009).

[13]   Eches, O., Dobigeon, N., et al., "An NCM-based Bayesian algorithm for hyperspectral unmixing", Hyperspectral Image and Signal Processing: Evolution in Remote Sensing, 2009. WHISPERS '09. First Workshop on, 1-4 (2009)

[14]   Nascimento, J. and Bioucas-Dias, J. M., "Learning dependent sources using mixtures of Dirichlet: Applications on hyperspectral unmixing", Hyperspectral Image and Signal Processing: Evolution in Remote Sensing, 2009. WHISPERS '09. First Workshop on, 1-5 (2009)

[15]   Zare, A., "Hyperspectral Endmember Detection and Band Selection Using Bayesian Methods", Computer & Information Science & Engineering, 136 (2008).

[16]   Zare, A. and Gader, P., "L1-Endmembers: A Robust Endmember Detection and Spectral Unmixing Algorithm", Proceedings of the SPIE Defense, Security, and Sensing, (2010).

[17]   Zare, A. and Gader, P. D., "Endmember detection using the Dirichlet process", Pattern Recognition, 2008. ICPR 2008. 19th International Conference on, 1-4 (2008)

[18]   Villeneuve, P. V., Gerstl, S. A., et al., "Estimating nonlinear mixing effects for arid vegetation scenes with MISR channels and observation directions", Geoscience and Remote Sensing Symposium Proceedings, 1998. IGARSS '98. 1998 IEEE International, 1234-1236 vol.3 (1998)

[19]   Han, T. and Goodenough, D. G., "Investigation of Nonlinearity in Hyperspectral Imagery Using Surrogate Data Methods", Geoscience and Remote Sensing, IEEE Transactions on, 46(10), 2840-2847 (2008).

[20]   Ainsworth, T. L., Bachmann, C. M., et al., "Local intrinsic dimensionality of hyperspectral imagery from non-linear manifold coordinates", Geoscience and Remote Sensing Symposium, 2007. IGARSS 2007. IEEE International, 1541-1542 (2007)

[21]   Bachmann, C. M., Ainsworth, T. L., et al., "Improvements to land-cover and invasive species mapping from hyperspectral imagery in the Virginia Coast reserve", Geoscience and Remote Sensing Symposium, 2004. IGARSS '04. Proceedings. 2004 IEEE International, 4180-4183 vol.6 (2004)

[22]   Bachmann, C. M., Ainsworth, T. L., et al., "Exploiting manifold geometry in hyperspectral imagery", Geoscience and Remote Sensing, IEEE Transactions on, 43(3), 441-454 (2005).

[23]   Bachmann, C. M., Ainsworth, T. L., et al., "Improved Manifold Coordinate Representations of Large-Scale Hyperspectral Scenes", Geoscience and Remote Sensing, IEEE Transactions on, 44(10), 2786-2803 (2006).

[24]   Bachmann, C. M., Ainsworth, T. L., et al., "Automated Estimation of Spectral Neighborhood Size in Manifold Coordinate Representations of Hyperspectral Imagery: Implications for Anomaly Finding, Bathymetry Retrieval, and Land Applications", Geoscience and Remote Sensing Symposium, 2008. IGARSS 2008. IEEE International, I-56-I-57 (2008)

[25]   Bachmann, C. M., Ainsworth, T. L., et al., "Bathymetric Retrieval From Hyperspectral Imagery Using Manifold Coordinate Representations", Geoscience and Remote Sensing, IEEE Transactions on, 47(3), 884-897 (2009).

[26]   Bachmann, C. M., Ainsworth, T. L., et al., "Manifold coordinate representations of hyperspectral imagery: Improvements in algorithm performance and computational efficiency", Geoscience and Remote Sensing Symposium (IGARSS), 2010 IEEE International, 4244-4247 (2010)

[27]   Bachmann, C. M., Ainsworth, T. L., et al., "A new data-driven approach to modeling coastal bathymetry from hyperspectral imagery using manifold coordinates", OCEANS, 2005. Proceedings of MTS/IEEE, 2242-2249 Vol. 3 (2005)

[28]   Bachmann, C. M., Ainsworth, T. L., et al., "Modeling Coastal Waters from Hyperspectral Imagery using Manifold Coordinates", Geoscience and Remote Sensing Symposium, 2006. IGARSS 2006. IEEE International Conference on, 356-359 (2006)

[29]   Baoxin, H., Miller, J. R., et al., "Investigation of linear spectral mixtures of the reflectance spectra using laboratory simulated forest scenes", Geoscience and Remote Sensing Symposium, 2002. IGARSS '02. 2002 IEEE International, 1535-1537 vol.3 (2002)

[30]   Borel, C. C. and Gerstl, S. A. W., "Nonlinear spectral mixing models for vegetative and soil surfaces", Remote Sensing of Environment, 47(3), 403-416 (1994).

[31]   Chen, X. and Vierling, L., "Spectral mixture analyses of hyperspectral data acquired using a tethered balloon", Remote Sensing of Environment, 103(3), 338-350 (2006).

[32]   Fan, W., Hu, B., et al., "Comparative Study Between a New Nonlinear Model and Common Linear Model for Analysing Laboratory Simulated-Forest Hyperspectral Data", International Journal of Remote Sensing, 30(11), 2951-2962 (2009).

[33]   Guilfoyle, K. J., Althouse, M. L., et al., "A quantitative and comparative analysis of linear and nonlinear spectral mixture models using radial basis function neural networks", Geoscience and Remote Sensing, IEEE Transactions on, 39(10), 2314-2318 (2001).

[34]   Halimi, A., Altmann, Y., et al., "Nonlinear Unmixing of Hyperspectral Images Using a Generalized Bilinear Model", Geoscience and Remote Sensing, IEEE Transactions on, PP(99), 1-10 (2011).

[35]   Heylen, R., Burazerovic, D., et al., "A graph-based method for non-linear unmixing of hyperspectral imagery", Geoscience and Remote Sensing Symposium (IGARSS), 2010 IEEE International, 197-200 (2010)

[36]   Heylen, R. and Scheunders, P., "Nonlinear barycentric dimensionality reduction", Image Processing (ICIP), 2010 17th IEEE International Conference on, 1341-1344 (2010)

[37]   Licciardi, G. A., "Neural Network Algorithms for Nonlinear Spectral Unmixing Applied on Hyperspectral Data", Hyperspectral 2010 Workshop, (2010).

[38]   Plaza, J., Martinez, P., et al., "Nonlinear Neural Network Mixture Models for Fractional Abundance Estimation in AVIRIS Hyperspectral Images", NASA Jet Propulsion Laboratory AVIRIS Airborne Earth Science Workshop, (2004).

[39]   Plaza, J., Plaza, A., et al., "Joint linear/nonlinear spectral unmixing of hyperspectral image data", Geoscience and Remote Sensing Symposium, 2007. IGARSS 2007. IEEE International, 4037-4040 (2007)

[40]   Poulet, F. and Erard, S., "Nonlinear spectral mixing: Quantitative analysis of laboratory mineral mixtures", J. Geophys. Res., 109(E2), E02009 (2004).

[41]   Rahman, M. T. and Alam, M. S., "Nonlinear Unmixing of Hyperspectral Data Using BDRF and Maximum Likelihood Algorithm", SPIE Automatic Target Recognition XVII, (2007)

[42]   Raksuntorn, N. and Qian, D., "Nonlinear mixture analysis for hyperspectral imagery", Geoscience and Remote Sensing Symposium,2009 IEEE International,IGARSS 2009, III-829-III-832 (2009)

[43]   Raksuntorn, N. and Qian, D., "Nonlinear Spectral Mixture Analysis for Hyperspectral Imagery in an Unknown Environment", Geoscience and Remote Sensing Letters, IEEE, 7(4), 836-840 (2010).

[44]   Ray, T. W. and Murray, B. C., "Nonlinear spectral mixing in desert vegetation", Remote Sensing of Environment, 55(1), 59-64 (1996).

[45]   Somers, B., Cools, K., et al., "Nonlinear Hyperspectral Mixture Analysis for tree cover estimates in orchards", Remote Sensing of Environment, 113(6), 1183-1193 (2009).

[46]   Wang, X. R., Kumar, S., et al., "Probabilistic Classification of Hyperspectral Images by Learning Nonlinear Dimensionality Reduction Mapping", Information Fusion, 2006 9th International Conference on, 1-8 (2006)

[47]   Weiwei, S. and Chun, L., "Manifold Coordinates Repairing of Boundary Points with PLS for Isomap Nonlinear Dimensionality Reduction of Hyperspectral Image", Multi-Platform/Multi-Sensor Remote Sensing and Mapping (M2RSM), 2011 International Workshop on, 1-6 (2011)

[48]   Wonkook, K., Yangchi, C., et al., "Multiresolution manifold learning for classification of hyperspectral data", Geoscience and Remote Sensing Symposium, 2007. IGARSS 2007. IEEE International, 3785-3788 (2007)

[49]   Wu, B., Zhang, L., et al., "Nonlinear Estimation of Hyperspectral Mixture Pixel Proportion Based on Kernel Orthogonal Subspace Projection", Advances in Neural Networks - ISNN 2006, 1070-1075 (2006).

[50]   Xuehong, C., Jin, C., et al., "Impact of collinearity on linear and nonlinear spectral mixture analysis", Hyperspectral Image and Signal Processing: Evolution in Remote Sensing (WHISPERS), 2010 2nd Workshop on, 1-4 (2010)

[51]   Yangchi, C., Crawford, M. M., et al., "Applying nonlinear manifold learning to hyperspectral data for land cover classification", Geoscience and Remote Sensing Symposium, 2005. IGARSS '05. Proceedings. 2005 IEEE International, 4311-4314 (2005)

[52]   Yangchi, C., Crawford, M. M., et al., "Improved Nonlinear Manifold Learning for Land Cover Classification via Intelligent Landmark Selection", Geoscience and Remote Sensing Symposium, 2006. IGARSS 2006. IEEE International Conference on, 545-548 (2006)

[53]   Mustard, J. F. and Pieters, C. M., "Quantitative Abundance Estimates From Bidirectional Reflectance Measurements", Journal of Geophysical Research, 92(B4), E617-E626 (1987).

[54]   Mustard, J. F. and Pieters, C. M., "Photometric Phase Functions of Common Geologic Minerals and Applications to Quantitative Analysis of Mineral Mixture Reflectance Spectra", Journal of Geophysical Research, 94(B10), 13619-13634 (1989).

[55]   Hapke, B. and Wells, E., "Bidirectional Reflectance Spectroscopy 2. Experiments and Observations", Journal of Geophysical Research, 86(B4), 3055-3060 (1981).

[56]   Hapke, B., [Theory of Reflectance and Emittance Spectroscopy], Cambridge University Press, (1993).

[57]   Nash, D. B. and Conel, J. E., "Spectral Reflectance Systematics for Mixtures of Powdered Hypersthene, Labradorite, and Ilmenite", Journal of Geophysical Research, 79(11), 1615-1621 (1974).

[58]   Singer, R. B. and McCord, T. B., "Mars: Large scale mixing of bright and dark surface materials and implications for analysis of spectral reflectance", Proc. Lunar Planet. Sci. Conf. 10th, 1835-1848 (1979).

[59]   Broadwater, J. and Banerjee, A., "A generalized kernel for areal and intimate mixtures", Hyperspectral Image and Signal Processing: Evolution in Remote Sensing (WHISPERS), 2010 2nd Workshop on, 1-4 (2010)

[60]   Broadwater, J. and Banerjee, A., "A comparison of kernel functions for intimate mixture models", Hyperspectral Image and Signal Processing: Evolution in Remote Sensing, 2009. WHISPERS '09. First Workshop on, 1-4 (2009)

[61]   Hapke, B., "Bidirectional Reflectance Spectroscopy 1. Theory", Journal of Geophysical Research, 86(B4), 3039-3054 (1981).

[62]   Shkuratov, Y., Starukhina, L., et al., "A Model of Spectral Albedo of Particulate Surfaces: Implications for Optical Properties of the Moon", Icarus, 137(2), 235-246 (1999).

[63]   Broadwater, J. and Banerjee, A., "Mapping Intimate Mixtures Using An Adaptive Kernel-Based Technique", Workshop on Hyperspectral Image and Signal Processing: Evolution in Remote Sensing, (2011).

[64]   Banerjee, A., Burlina, P., et al., "A machine learning approach for finding hyperspectral endmembers", Geoscience and Remote Sensing Symposium, 2007. IGARSS 2007. IEEE International, 3817-3820 (2007)

[65]   Broadwater, J., Chellappa, R., et al., "Kernel fully constrained least squares abundance estimates", Geoscience and Remote Sensing Symposium, 2007. IGARSS 2007. IEEE International, 4041-4044 (2007)

[66]   Bachmann, C. M. and Ainsworth, T. L., "Bathymetric retrieval from manifold coordinate representations of hyperspectral imagery", Geoscience and Remote Sensing Symposium, 2007. IGARSS 2007. IEEE International, 1548-1551 (2007)

[67]   Bachmann, C. M., Ainsworth, T. L., et al., "Improved manifold coordinate representations of hyperspectral imagery", Geoscience and Remote Sensing Symposium, 2005. IGARSS '05. Proceedings. 2005 IEEE International, 4307-4310 (2005)

[68]   Dong, G., Zhang, Y., et al., "Dimensionality Reduction of Hyperspectral Data Based on ISOMAP Algorithm", Electronic Measurement and Instruments, 2007. ICEMI '07. 8th International Conference on, 3-935-3-938 (2007)

[69]   Jinhuan, W., Zheng, T., et al., "Feature extraction of hyperspectral images based on preserving neighborhood discriminant embedding", Image Analysis and Signal Processing (IASP), 2010 International Conference on, 257-262 (2010)

[70]   Karantzalos, K., "Intrinsic dimensionality estimation and dimensionality reduction through scale space filtering", Digital Signal Processing, 2009 16th International Conference on, 1-6 (2009)

[71]   Kuybeda, O., Malah, D., et al., "Anomaly Preserving $\ell_{2,\infty}$-Optimal Dimensionality Reduction Over a Grassmann Manifold", Signal Processing, IEEE Transactions on, 58(2), 544-552 (2010).

[72]   Li, M., Crawford, M. M., et al., "Anomaly detection for hyperspectral images using local tangent space alignment", Geoscience and Remote Sensing Symposium (IGARSS), 2010 IEEE International, 824-827 (2010)

[73]   Ling, C., Rui, H., et al., "Graph-based semi-supervised weighted band selection for classification of hyperspectral data", Audio Language and Image Processing (ICALIP), 2010 International Conference on, 1123-1126 (2010)

[74]   Merenyi, E., Csatho, B., et al., "Knowledge discovery in urban environments from fused multi-dimensional imagery", Urban Remote Sensing Joint Event, 2007, 1-13 (2007)

[75]   Velasco-Forero, S., Angulo, J., et al., "Morphological image distances for hyperspectral dimensionality exploration using Kernel-PCA and ISOMAP", Geoscience and Remote Sensing Symposium,2009 IEEE International,IGARSS 2009, III-109-III-112 (2009)

[76]   Yuan, Z., Bo, W., et al., "Edge detection on hyperspectral imagery via Manifold techniques", Hyperspectral Image and Signal Processing: Evolution in Remote Sensing, 2009. WHISPERS '09. First Workshop on, 1-4 (2009)

[77]   Li, M., Crawford, M. M., et al., "Local Manifold Learning-Based k -Nearest-Neighbor for Hyperspectral Image Classification", Geoscience and Remote Sensing, IEEE Transactions on, 48(11), 4099-4109 (2010).

[78]   Wei, D. and Crawford, M. M., "Locally consistent graph regularization based active learning for hyperspectral image classification", Hyperspectral Image and Signal Processing: Evolution in Remote Sensing (WHISPERS), 2010 2nd Workshop on, 1-4 (2010)

[79]   Wonkook, K. and Crawford, M., "A novel adaptive classification method for hyperspectral data using manifold regularization kernel machines", Hyperspectral Image and Signal Processing: Evolution in Remote Sensing, 2009. WHISPERS '09. First Workshop on, 1-4 (2009)

[80]   Wonkook, K. and Crawford, M. M., "Adaptive Classification for Hyperspectral Image Data Using Manifold Regularization Kernel Machines", Geoscience and Remote Sensing, IEEE Transactions on, 48(11), 4110-4121 (2010).

[81]   Wonkook, K., Crawford, M. M., et al., "Spatially Adapted Manifold Learning for Classification of Hyperspectral Imagery with Insufficient Labeled Data", Geoscience and Remote Sensing Symposium, 2008. IGARSS 2008. IEEE International, I-213-I-216 (2008)

[82]   Heylen, R., Burazerovic, D., et al., "Non-linear Spectral Unmixing by Geodesic Simplex Volume Maximization", Selected Topics in Signal Processing, IEEE Journal of, PP(99), 1-1 (2010).

[83]   Nascimento, J. M. P. and Bioucas-Dias, J. M., "Unmixing Hyperspectral Intimate Mixtures", SPIE Image and Signal Processing for Remote Sensing XVI, (2010)

[84]   Johnson, P. E., Smith, M. O., et al., "Quantitative Analysis of Planetary Reflectance Spectra with Principal Components Analysis", Journal of Geophysical Research, 90(C805-C810 (1985).

[85]   Smith, M. O., Johnson, P. E., et al., "Quantitative Determination of Mineral Types and Abundances from Reflectance Spectra Using Principal Components Analysis", Journal of Geophysical Research, 90(Supplement), C797-C804 (1985).

[86]   Close, R., Gader, P., et al., "Hyperspectral Unmixing Using Macroscopic and Microscopic Mixture Models", IEEE Journal of Selected Topics in Applied Earth Observations and Remote Sensing [under review], (2012).

[87]   Manolakis, D., Marden, D., et al., "Hyperspectral Image Processing for Automatic Target Detection Applications", Lincoln Laboratory Journal, 14(1), 79-116 (2003).

[88]   Haykin, S., [Neural Networks and Learning Machines], Pearson Education, Inc., (2009).